

“Wet” Versus “Dry” Folding of Polyproline

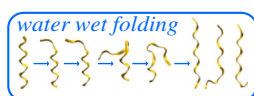
Liuqing Shi,¹ Alison E. Holliday,² Brian C. Bohrer,³ Doyong Kim,⁴ Kelly A. Servage,⁴ David H. Russell,⁴ David E. Clemmer¹

¹Department of Chemistry, Indiana University, Bloomington, IN 47405, USA

²Department of Chemistry, Moravian College, Bethlehem, PA 18018, USA

³Department of Chemistry, University of Southern Indiana, Evansville, IN 47712, USA

⁴Department of Chemistry, Texas A&M University, College Station, TX 77843, USA



Abstract. When the all-*cis* polyproline-I helix (PPI, favored in 1-propanol) of polyproline-13 is introduced into water, it folds into the all-*trans* polyproline-II (PPII) helix through at least six intermediates [Shi, L., Holliday, A.E., Shi, H., Zhu, F., Ewing, M.A., Russell, D.H., Clemmer, D.E.: Characterizing intermediates along the transition from PPI to PPII using ion mobility-mass spectrometry. *J. Am. Chem. Soc.* 136, 12702–12711 (2014)]. Here, we show that the solvent-free intermediates refold to the all-*cis* PPI helix with high (>90%) efficiency. Moreover, in the absence of solvent, each intermediate appears to utilize the same small set of pathways observed for the solution-phase PPII → PPI transition upon immersion of PPII_{aq} in 1-propanol. That folding in solution (under conditions where water is displaced by propanol) and folding in vacuo (where energy required for folding is provided by collisional activation) occur along the same pathway is remarkable. Implicit in this statement is that 1-propanol mimics a “dry” environment, similar to the gas phase. We note that intermediates with structures that are similar to PPII_{aq} can form PPII under the most gentle activation conditions—indicating that some transitions observed in water (i.e., “wet” folding, are accessible (albeit inefficient) in vacuo. Lastly, these “dry” folding experiments show that PPI (all *cis*) is favored under “dry” conditions, which underscores the role of water as the major factor promoting preference for *trans* proline.

Keywords: Folding, Collisional activation

Received: 4 December 2015/Revised: 20 February 2016/Accepted: 22 February 2016/Published Online: 8 April 2016

Introduction

The *cis*-to-*trans* isomerization of proline plays a critical role in altering biomolecular configurations [1–4], and proline-rich segments frequently occur in dynamic regions of biomolecules [4–7]. Since the 1955 crystal structure for the all-*trans* polyproline-II (PPII) helix [8], polyproline has become a textbook example of how solvent influences structure [9, 10]. Sela and co-workers [11] and Katchalski et al. [12, 13] first reported experimental data that revealed an all *cis* structure for polyproline in aliphatic alcohols, and the crystal structure for the all-*cis* polyproline-I (PPI) was reported in 1963 [14]. Since this time, the interconversion between these helical structures has continued to attract substantial experimental [15–18] and theoretical [19–22] attention. Although *cis* and *trans* proline configurations are energetically similar, differing by

~10 kcal·mol⁻¹, there exists a substantial (~20 kcal·mol⁻¹) free energy barrier to their interconversion [23]; however, the proline *cis*-to-*trans* isomerization reaction can be intramolecularly catalyzed by hydrogen bonding interactions as well as post-translational modifications [23]. The all-*trans* PPII helix is stabilized through interactions of water molecules with carbonyl groups along the peptide backbone [14, 24–26].

Recently, we examined the kinetics and thermodynamics of structural transitions associated with a 13-residue polyproline (Pro13) interconverting between the PPI and PPII helices in different solution environments [27, 28]. When PPI_{PrOH} is immersed in water, the peptide undergoes a spontaneous, step-wise folding transition through six intermediates as it folds into the PPII_{aq} form [27]. Because the reaction sequence is initiated upon addition of water, we refer to it as “wet” folding. Alternatively, when the hydrated PPII_{aq} helix is immersed in 1-propanol, multiple *cis/trans*-configured intermediates are formed in parallel. These different structures subsequently undergo folding transitions and converge through a series of

Correspondence to: David H. Russell; e-mail: russell@chem.tamu.edu, David E. Clemmer; e-mail: Clemmer@Indiana.EDU

intermediates en route to forming the PPI_{PrOH} helix [28]. As the observed structural transitions are a direct result of the dehydration process associated with the displacement of water by 1-propanol, the PPII_{aq} → PPI_{PrOH} transition is referred to as a “dry” solution-folding. The previously published kinetics data, used to determine each of these solution-phase folding mechanisms, are summarized in Figure 1. As explained in the figure, the kinetics fits are extremely sensitive to the employed model, allowing for delineation of detailed folding pathways [27, 28].

Although much is now known about peptide and protein structures in solution, little is known about non-native states (e.g., unstructured, denatured, and intermediate forms) that must exist as biopolymers respond to changes in environment. In recent years, soft ionization techniques, such as electrospray [29], have made it possible to study biopolymer structures in the absence of solvent. In some cases, it appears that evaporative cooling associated with desolvating molecules effectively “freeze-dries” populations of states that were present in

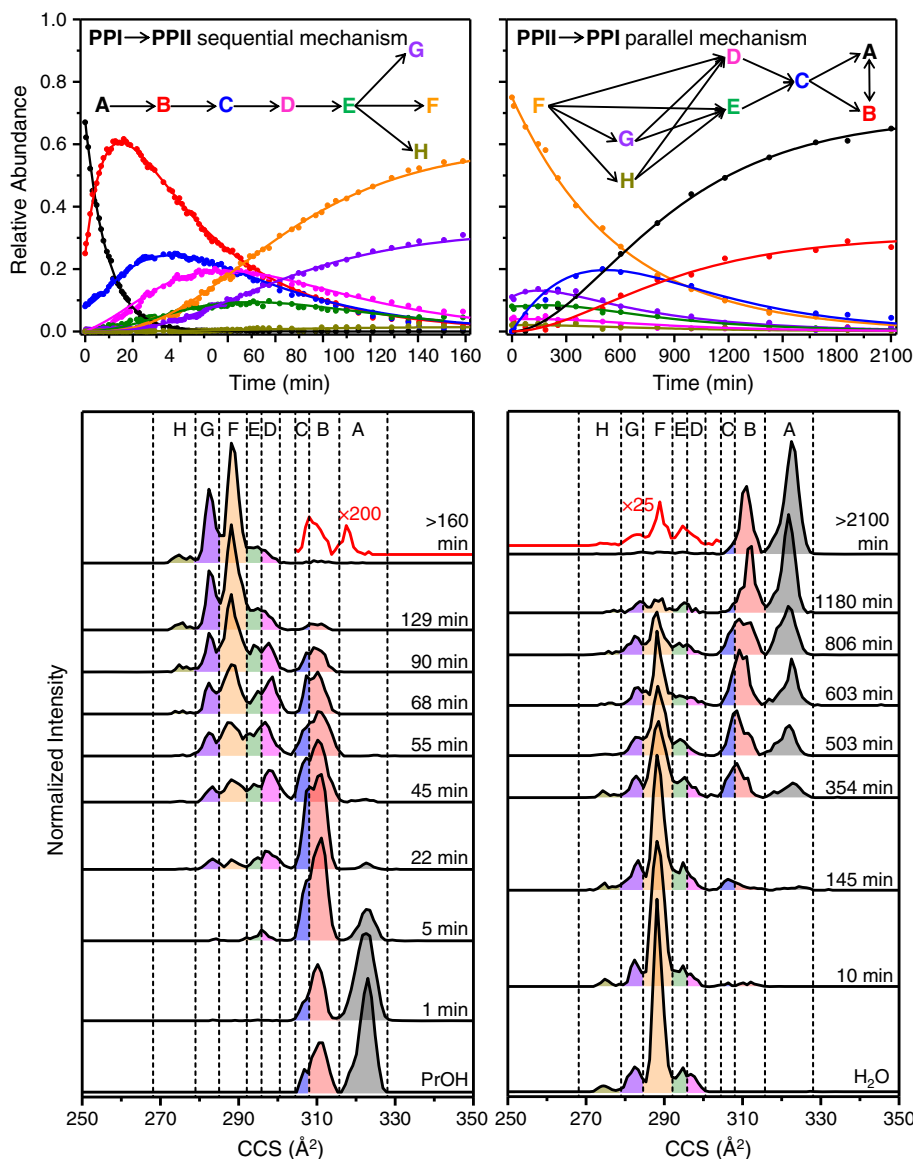


Figure 1. Kinetic data of Pro13 in different solution environments at 23 °C, showing the PPI → PPII transition in 10:88:2 1-propanol:H₂O:HOAc (v:v:v) (left side) and the PPII → PPI transition in 97:1:2 1-propanol:H₂O:HOAc(v:v:v) (right side) (taken from ref 28). For both directions, eight different conformational types (A-H) are resolved and assigned. Top: Relative abundances of different conformers as a function of transition time. Each abundance profile is determined by integrating the regions of the spectra associated with specific conformational types, and kinetic fitting is performed for each relative abundance curve based on the first-order reaction rate laws. The shown transition mechanisms give the best fit to the experimental data. Bottom: Example collision cross section (CCS) distributions for Pro13 [M + 2H]²⁺ ions at different transition time points. Dashed lines delineate the cross section region for each conformer, and the inset (red) shows a blow up of low-abundance species present at equilibrium. Various colors are used to represent different conformations: black is conformer A, red is conformer B, blue is conformer C, magenta is conformer D, olive is conformer E, orange is conformer F, violet is conformer G, and dark yellow is conformer H

solution [30–36]. It is quite common to see multiple structural forms of an ionized biomolecule in the absence of solvent, but the relationship of such states to solution-phase structures remains largely uncharacterized by experimental techniques. As a system, polyproline is especially interesting because it can be studied using a range of environments and, as described above, very different structural forms are known. In vacuo studies of such systems provide the opportunity to understand how intramolecular interactions, intrinsic to the biomolecule, influence structure [37–41]. When compared with solution folding experiments, it is possible to gain an understanding of the role of solvent in inducing structural transitions.

In this paper, we use collisional activation studies to investigate transitions of solvent-free forms of intermediates that are formed by electrospray during the $\text{PPI}_{\text{PrOH}} \rightarrow \text{PPII}_{\text{aq}}$ “wet” folding transition (Figure 2). Intermediates are formed upon solvent exchange into water, and when activated in vacuo, conformational changes are observed as a function of activation energy. Notable similarities between the in vacuo mechanism and the $\text{PPII}_{\text{aq}} \rightarrow \text{PPI}_{\text{PrOH}}$ “dry” solution transition induced upon exchange of water for 1-propanol reveals that

removal of water is key to folding. In vacuo conditions are effectively mimicking a nonpolar solution environment. Conversely, the “dry” folding mechanism further illustrates the key role of water as the major factor promoting the well-known preferences for *trans* proline [24–27].

Experimental

Instrumentation

Experiments were performed on a prototype ion mobility spectrometry (IMS) time-of-flight (TOF) mass spectrometry (MS) instrument. A schematic of the instrument used in this work is shown in Figure 2. IMS theory and instrumentation have been described in detail previously [42–52]; a brief description is given here. Ions were produced via electrospray ionization (ESI) by a chip-based autosampler (Advion, Ithaca, NY, USA) and accumulated in an hourglass-shaped ion funnel, F1 [53]. A 150 μs -wide electrostatic gate (G1) was used to periodically release ions into the drift region (D1 and D2). Under the influence of a uniform electric field ($\sim 10 \text{ V} \cdot \text{cm}^{-1}$), ions

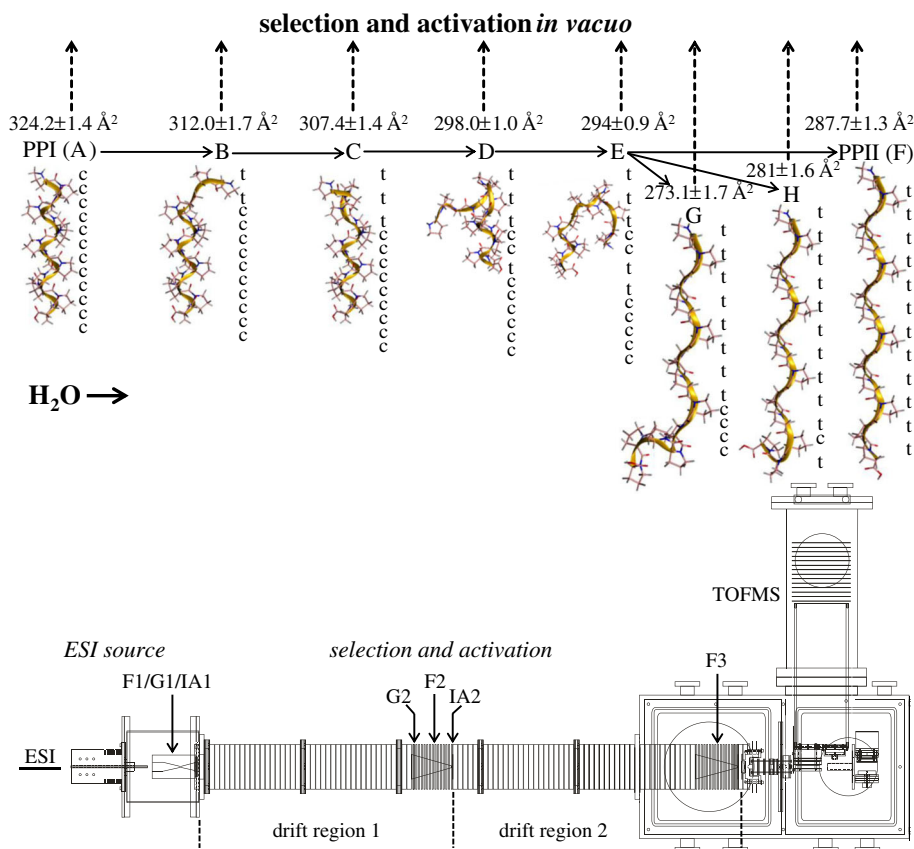


Figure 2. Top: A sequential transition mechanism proposed for the $\text{PPI} \rightarrow \text{PPII}$ conversion of Pro13 in aqueous environment (ref 27). The structures of all the eight conformers found during the transition process, as well as the assignment of the *cis(c)/trans(t)* configurations of peptide bonds of each solution conformer, are also provided. In this work, each solution conformation of Pro13 that exists during the $\text{PPI}_{\text{PrOH}} \rightarrow \text{PPII}_{\text{aq}}$ transition process is electrosprayed into the gas phase, selected, and gently collisional activated in order to investigate the folding of Pro13 in vacuo. Bottom: Schematic diagram of the IMS-IMS-TOF instrument used to select and activate conformations of Pro13 $[\text{M} + 2\text{H}]^{2+}$ ions. The instrument includes an ESI source, a $\sim 1.8 \text{ m}$ drift tube (D1 and D2), and a TOF mass spectrometer

were separated on the basis of their mobilities while migrating through the drift region filled with ~ 3 Torr of He (300 K). In the middle of the drift tube, funnel F2 radially focuses the diffuse ion packet and includes an electrostatic gate (G2) and activation region (IA2). Ions are again focused through funnel F3 after separation through D2. Upon exiting the drift region, ions enter an orthogonal-extraction TOF-MS for nested drift time (t_D) and mass-to-charge (m/z) measurement [54].

IMS Measurements

Two operational modes of the instrument shown in Figure 2 were used in this work: one-dimensional (IMS-MS) and two-dimensional (IMS-IMS-MS). Detailed instrumentation for the IMS-MS and IMS-IMS-MS experiments has been discussed elsewhere [54–58]; only a brief description is provided here. The drift tube is divided into two effective drift regions (D1 and D2) by ion funnel F2. The source mobility distributions were obtained in the IMS-MS mode, wherein the field in G2 allows all ions separated through the first drift region D1 to pass into the second drift region D2. In this case, D1 and D2 are operated as a uniform, ~ 1.8 -m drift tube.

The ion mobility distributions of the activated ions were measured under the IMS-IMS-MS mode, wherein D1 and D2 are operated as two independent drift regions of 0.84 and 0.98 m, respectively. In these experiments, after ions travel through D1, ions of a desired mobility are selected to pass through G2 by applying a delay pulse to G2 to lower a repulsive potential (16 V) for 30–100 μ s. The delay pulse at G2 is triggered by the initial pulse at G1 in order to isolate ions with a specific mobility from the source distribution. All other ions are neutralized on the first lens of G2. After passing through the gate region G2, a narrow range of mobility-selected ions continue to travel through funnel F2 and are then activated by undergoing gentle collisions with the buffer gas in the IA2 region. Collisional activation is achieved by applying an additional voltage drop across the two lenses of IA2 that are ~ 3 mm apart, and the energetics of these collisions is directly influenced by the magnitude of the voltage drop across IA2. As ions leave the activation region, they are rapidly thermalized to the temperature of the buffer gas (300 K) and are subsequently separated in the second drift region, D2. For each selected conformer, the same IMS distribution was used as the source distribution for all the spectra collected under the IMS-IMS mode, and the IMS-IMS distributions were recorded over an activation voltage range of 6 V to 200 V.

Determination of Experimental Collision Cross Sections

Experimental collision cross sections (Ω) can be determined from ion drift time (t_D) using Eq. 1. [46],

$$\Omega = \frac{(18\pi)^{1/2}}{16} \frac{ze}{(k_b T)^{1/2}} \left[\frac{1}{m_I} + \frac{1}{m_B} \right]^{1/2} \frac{t_D E}{L} \frac{760}{P} \frac{T}{273.2} \frac{1}{N} \quad (1)$$

where ze , k_b , and T correspond to the ion's charge, Boltzmann's constant, and the temperature of the buffer gas, respectively. m_I is the mass of the ion, m_B is the mass of the buffer gas, and N is the neutral number density of the buffer gas at STP. E , L , P refer to the applied electric field, the length of the drift region, and the buffer gas pressure, respectively. Uncertainties of the experimental collision cross sections correspond to one deviation about the mean for three independent measurements.

Sample Preparation

The Pro13 peptide was synthesized on a modified Applied Biosystems 430A synthesizer (Applied Biosystems, Foster City, CA, USA). A standard Boc solid-phase peptide synthesis protocol was used by following the same procedure described previously [27, 59].

The Pro13 peptide was initially dissolved in pure 1-propanol at a concentration of 160 μ M and incubated at 37 $^{\circ}$ C for at least 72 h to ensure that all peptides were in the PPI configuration. The PPI \rightarrow PPII transition at 23 $^{\circ}$ C was initiated by diluting the incubated PrOH stock solution to a final composition of 10:88:2 PrOH:H₂O:HOAc (v:v:v) containing 16 μ M Pro13, as described previously [27]. The source distributions for conformers A–C and D–H were obtained 1 min and 180 min, respectively, after the transition was induced.

Assignment of Peaks and Structures

Upon electrospraying a PrOH:H₂O solvent mixture, the dominant ion formed by Pro13 is $[M + 2H]^{2+}$. Once the PPI \rightarrow PPII transition is initiated, eight different structural types (A–H) are resolved and assigned for Pro13 $[M + 2H]^{2+}$ ions during the transition process [27]. As is summarized in Figures 1 and 2, a sequential transition mechanism involving six different intermediates has been proposed for the PPI_{PrOH} \rightarrow PPII_{aq} conversion [27]. Figure 2 also shows the experimental collision cross section of each conformer, as well as the assignment of the *cis/trans* peptide bonds along the backbone, as determined using molecular modeling studies [27]. In this study, no new structural feature was discovered upon activation of each selected conformation; therefore, the conformational types observed in the IMS-IMS distributions were assigned on the basis of the experimental collision cross section determined in prior IMS-MS work [27]. More detailed discussion is given below.

Generation of the Relative Abundance Profiles

The relative abundance profile of all observed conformers as a function of activation voltage was determined for each selected conformation. This was achieved using the Peak Analyzer tool in OriginPro 9.0.0 (OriginLab Corporation, Northampton, MA, USA). Dashed lines shown in Figures 3 and 4 delineate the collision cross section region for each conformer type,

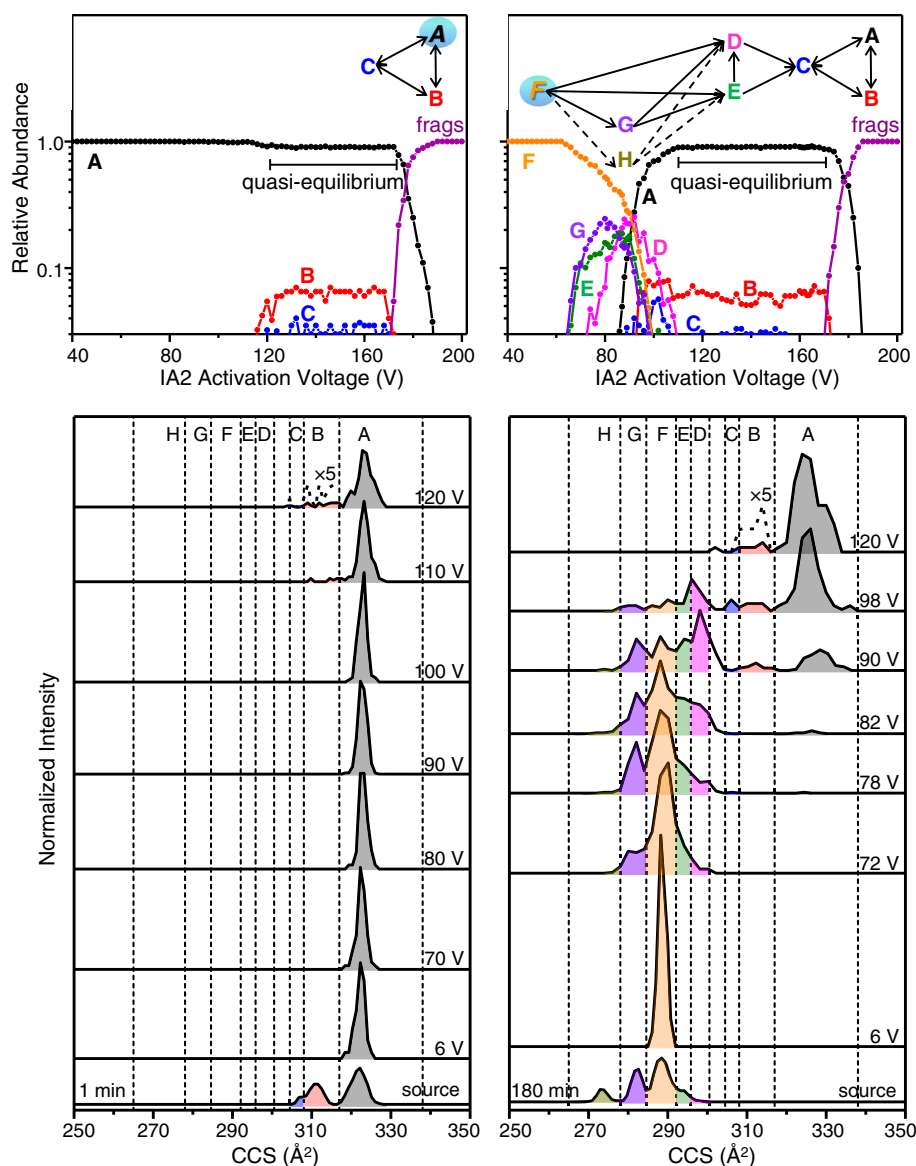


Figure 3. Selection and activation data of Pro13 $[M + 2H]^{2+}$ ions when conformer A (left side) and conformer F (right side) are selected. Top: Relative abundance as a function of activation voltage. The observed transition mechanism of each conformer upon activation in vacuo is also shown. A dashed arrow represents a possible transition pathway that may exist but is not observed experimentally. The bracketed line denotes the quasi-equilibrium region prior to fragmentation. Bottom: Representative collision cross section (CCS) distributions of initial selection (6 V) and activation up to 120 V. The bottom trace in each panel shows the source distribution obtained at the relevant solution-phase PPI \rightarrow PPII transition time, and the inset (dashed) shows a blow up of low-abundance species present at quasi-equilibrium. Dashed lines delineate the cross section region for each conformer. Color coding for each conformer is the same as Figure 1, and dark purple represents the relative abundance of all observed fragment populations (frags) originating from the selected ions

as has been assigned previously [27]. It is worth noting that upon activation of each selected conformer, only the second drift region (D2) is available for separation, resulting in a lower resolution in the mobility distribution. Therefore, dashed lines associated with the regions of conformers A and H are adjusted, since the A and H peaks are noticeably broader compared with those assigned previously [27]. According to the abundance profiles, putative transition routes in vacuo were proposed for each selected conformer.

Results and Discussion

Selection and Activation of the 1-Propanol-Precursor PPI_{PrOH} and Aqueous-Product PPII_{aq} Helices

In prior work, we found that eight different solution structures (A–H) are resolved during the *wet*-folding PPI_{PrOH} \rightarrow PPII_{aq} transition [27]. In this work, these structures are electrosprayed into the gas-phase, selected, and activated. We begin by considering the $[PPI + 2H]^{2+}$ (peak A, sampled after immersion in

water for 1 min) and $[\text{PPII} + 2\text{H}]^{2+}$ (peak F, sampled after immersion in water for 180 min) species formed from the solution-phase 1-propanol precursor PPI_{PrOH} and aqueous-product PPII_{aq} helices. This analysis provides key information about what structures are accessible when folding is initiated in the absence of solvent. We follow this discussion with brief analyses of each of the solution intermediates.

Several mobility distributions for activation of $[\text{PPI} + 2\text{H}]^{2+}$ and $[\text{PPII} + 2\text{H}]^{2+}$ ions are shown in Figure 3. One minute after immersion in water, we observe that PPI (peak A), is present at a substantial abundance ($63\% \pm 4\%$) in the source distribution. The early $\text{PPI}_{\text{PrOH}} \rightarrow \text{PPII}_{\text{aq}}$ solution intermediates B and C are also present. Selection and activation of peak A shows essentially no change in the mobility distribution over an activation voltage of 0 V to 120 V. At ~ 110 V, peak A begins to decrease in intensity, and by 120 V, peak A has decreased to $91\% \pm 3\%$ of the distribution, and very small amounts of structures B ($6\% \pm 2\%$) and C ($3\% \pm 2\%$) are observed. The presence of these new structures indicates that some of the $[\text{PPI} + 2\text{H}]^{2+}$ ions have been collisionally activated above the barrier for formation of structures B and C. Peaks A, B, and C are the only states that are observed upon activation of $[\text{PPI} + 2\text{H}]^{2+}$. That is, *all other states observed as intermediates in the $\text{PPI}_{\text{PrOH}} \rightarrow \text{PPII}_{\text{aq}}$ transformation in solution (D–H) are inaccessible in the absence of solvent upon activating peak A $[\text{PPI} + 2\text{H}]^{2+}$ ions.*

Figure 3 also shows the integrated signals for the A, B, and C regions as a function of voltage. Close examination of these data indicates that conformations B and C have almost identical threshold voltages (~ 108 V) for formation from A. As the activation voltage is increased, the abundance of the B and C products increases and then the populations of all three states remain constant over a wide activation voltage range, ~ 120 V to 170 V. This flat region is indicative of a quasi-equilibrium in the gas phase involving the A, B, and C states [58]. That is, when the ions are above all barriers that separate the A, B, and C states, the distribution from ~ 120 V to ~ 170 V reflects the local equilibrium populations of these states. Above 170 V, all of the species in the quasi-equilibrium distribution of ions begin to dissociate. Regardless of which conformer is selected for activation in these experiments, the ratios of abundant fragment ions appear to be identical. The populations of A, B, and C structures decrease as fragment ion populations increase and eventually dominate the distribution at higher voltage (> 180 V). The simple schematic in Figure 3 shows our interpretation of these data: at relatively low activation energies, A will convert to B and C; at higher energies, the A, B, and C states coexist as a quasi-equilibrium distribution of states. This quasi-equilibrium distribution favors A (or PPI).

Figure 3 also shows the distribution of structures formed upon activation of $[\text{PPII} + 2\text{H}]^{2+}$ (i.e., peak F sampled from solution after PPI_{PrOH} was immersed in water for 180 min). This distribution is quite different from the data recorded for activation of peak A, especially at low voltages. Mobility distributions as a function of activation energy show that $[\text{PPII} + 2\text{H}]^{2+}$ ions (peak F) begin to form other structures at much lower activation voltages (~ 65 V) through what appears to be a

complex set of transitions. The first transition is observed when ions are activated with ~ 65 V. Conformer F ($\Omega = 287.7 \pm 1.3 \text{ \AA}^2$) first forms the more compact conformer G ($\Omega = 281 \pm 1.6 \text{ \AA}^2$). Slightly above this voltage (~ 67 V), conformer F forms the slightly larger E state ($\Omega = 294 \pm 0.9 \text{ \AA}^2$). The populations of these new structures increase with increasing activation voltage until conformer D (which is even more elongated, with $\Omega = 298.0 \pm 1.0 \text{ \AA}^2$) is observed at ~ 77 V. As the fraction of D increases, the abundances of the G and E peaks decrease. This behavior indicates that G and E are intermediates to forming D (i.e., $F \rightarrow G \rightarrow D$ and $F \rightarrow E \rightarrow D$). At higher energies, a very small fraction of ions may be present in the region associated with conformation H. This suggests that this product might be accessible upon activation of F in the absence of solvent. However, it is such a minor process that we ignore it as an important pathway upon activation of F.

Unlike $[\text{PPI} + 2\text{H}]^{2+}$ (peak A), which showed little structural variance upon activation, $[\text{PPII} + 2\text{H}]^{2+}$ (peak F) was able to access a number of intermediate states en route to forming its final structure. The integrated population distribution in Figure 3 shows that as soon as A is formed from the initial activation of F (~ 80 V), the population of peak D and remaining populations of G and E decrease rapidly until they fall below our detection limits. In the same voltage region, the abundances of conformers B and C increase slightly. Thus, it appears that D, G, and E may all be intermediates along the pathway to forming peak A in vacuo, the $[\text{PPI} + 2\text{H}]^{2+}$ species. Remarkably, this suggests that the $\text{PPII} \rightarrow \text{PPI}$ folding pathway in solvent (1-propanol) and in the gas phase are similar. As the activation energy is increased even further (116–170 V), the F precursor and intermediates D–H disappear and the gas-phase quasi-equilibrium distribution is observed. Above ~ 170 V, the A, B, and C populations are depleted as ions dissociate.

This analysis provides substantial insight into the in vacuo $\text{PPII} \rightarrow \text{PPI}$ folding mechanism. The low energy formation of G and then E followed by formation of D indicates that in vacuo, the F state folds via a parallel mechanism using multiple pathways to produce the intermediates D, E, and G. In addition, the observation that conformers B and C appear as soon as peak A is formed at relatively higher activation voltage implies that there is a critical barrier for the compact intermediates D, E, and G to produce the quasi-equilibrium populations (i.e., a common transition state must be produced before the A–C states start to form). These findings appear to be analogous to those elucidated for the solution-phase $\text{PPII}_{\text{aq}} \rightarrow \text{PPI}_{\text{PrOH}}$ dry folding transition (shown in Figure 1). The inset in Figure 3 shows a pathway that is consistent with these data.

One final point involves the timescale of these transitions. Consider the $F \rightarrow A$ transition. If a substantial amount of time was required to complete the conformational change, we would observe a shift in the product mobility distribution of peak A to shorter drift times. Any shift associated with the experimental time required for $F \rightarrow A$ is below the smallest, 50 μs , time interval used to record the IMS distributions. Thus, $\tau(F \rightarrow A) \leq 50 \mu\text{s}$. Such a fast transition is expected at the elevated energies that are sampled during collisional activation. Additionally, in

the complete absence of solvent, the barriers associated with solvent reorganization are eliminated. Thus, while ~ 3 h is required for PPI_{PrOH} to form PPII_{aq} upon immersion of PPI in water, the solvent-free, collisionally activated PPII instantaneously snaps back to the PPI state ($\tau \leq 50$ μs) with high ($>90\%$) efficiency.

Selection and Activation of Solution Intermediate B

More insight about the gas-phase folding process comes from studies of each of six solution intermediates (conformers B, C, D, E, G, and H) that are formed during the “wet” solution-folding transition $\text{PPI}_{\text{PrOH}} \rightarrow \text{PPII}_{\text{aq}}$. Each of these structures is formed in the gas phase using ESI and then selected and collisionally activated as described above. Ion mobility

distributions obtained at different activation voltages after selection of B, C, D, E, G, and H individually are shown in Figure 4, whereas plots of the integrated data are shown in Figure 5. Conformers B and C are selected and activated from solution after the immersion of PPI_{PrOH} stock solution in water for 1 min, whereas the D, E, G, and H states are sampled from solution after PPI_{PrOH} was immersed in water for 180 min.

As is shown in Figure 4, activation of the B intermediate at 120 V effectively results in the same quasi-equilibrium distribution as that observed at high activation voltages for the $[\text{PPI} + 2\text{H}]^{2+}$ (peak A) and $[\text{PPII} + 2\text{H}]^{2+}$ (peak F) species. Before reaching quasi-equilibrium, conformer B displays no significant conformational changes at low activation voltages. However, upon increasing the activation voltage (e.g., to 82 V as shown in Figure 4), conformers A and C are produced from

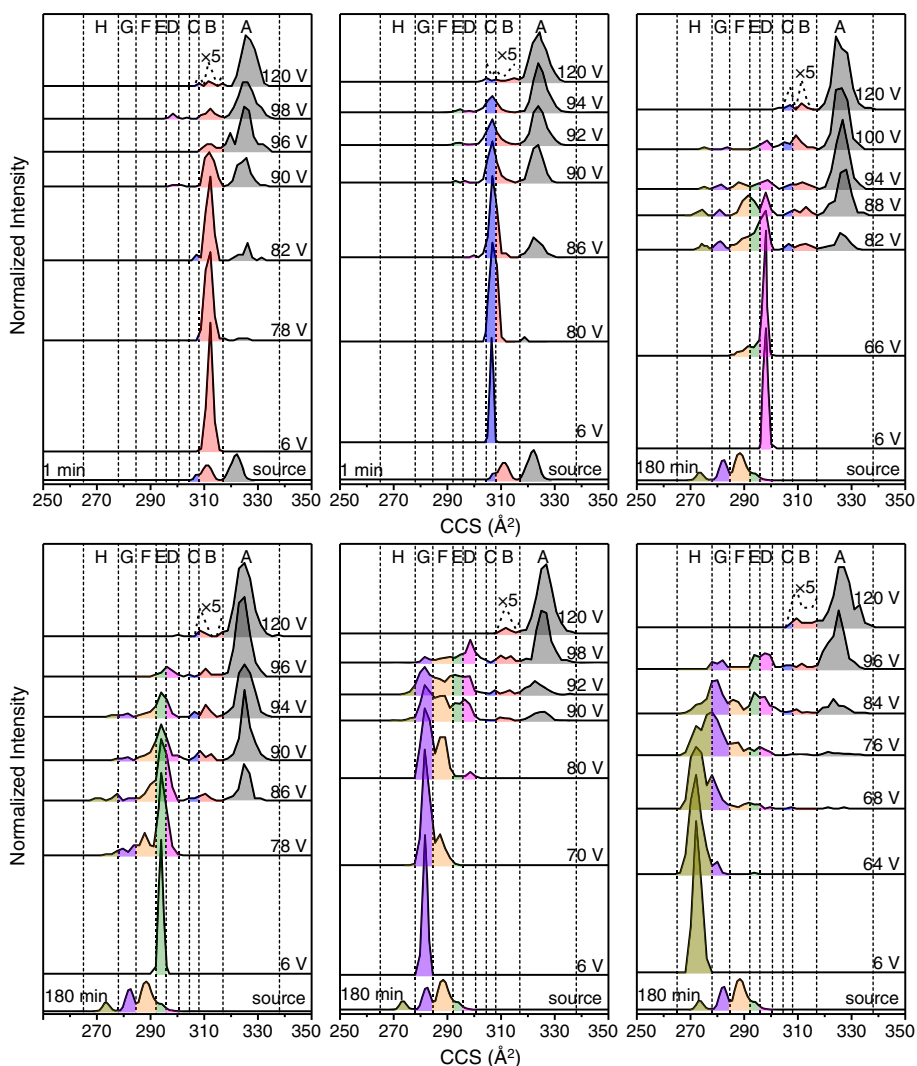


Figure 4. Representative collision cross section (CCS) distributions of Pro13 $[\text{M} + 2\text{H}]^{2+}$ ions when six different solution intermediates are selected and activated: B (top left), C (top middle), D (top right), E (bottom left), G (bottom middle), and H (bottom right). For each conformer, initial selection occurs at 6 V, and the activation voltage is increased up to 120 V. The bottom trace in each panel shows the source distribution obtained at the relevant solution-phase $\text{PPI} \rightarrow \text{PPII}$ transition time, and the inset (dashed) shows a blow up of low-abundance species present at quasi-equilibrium. Dashed lines delineate the cross section region for each conformer, and color coding for each conformer is the same as Figure 1

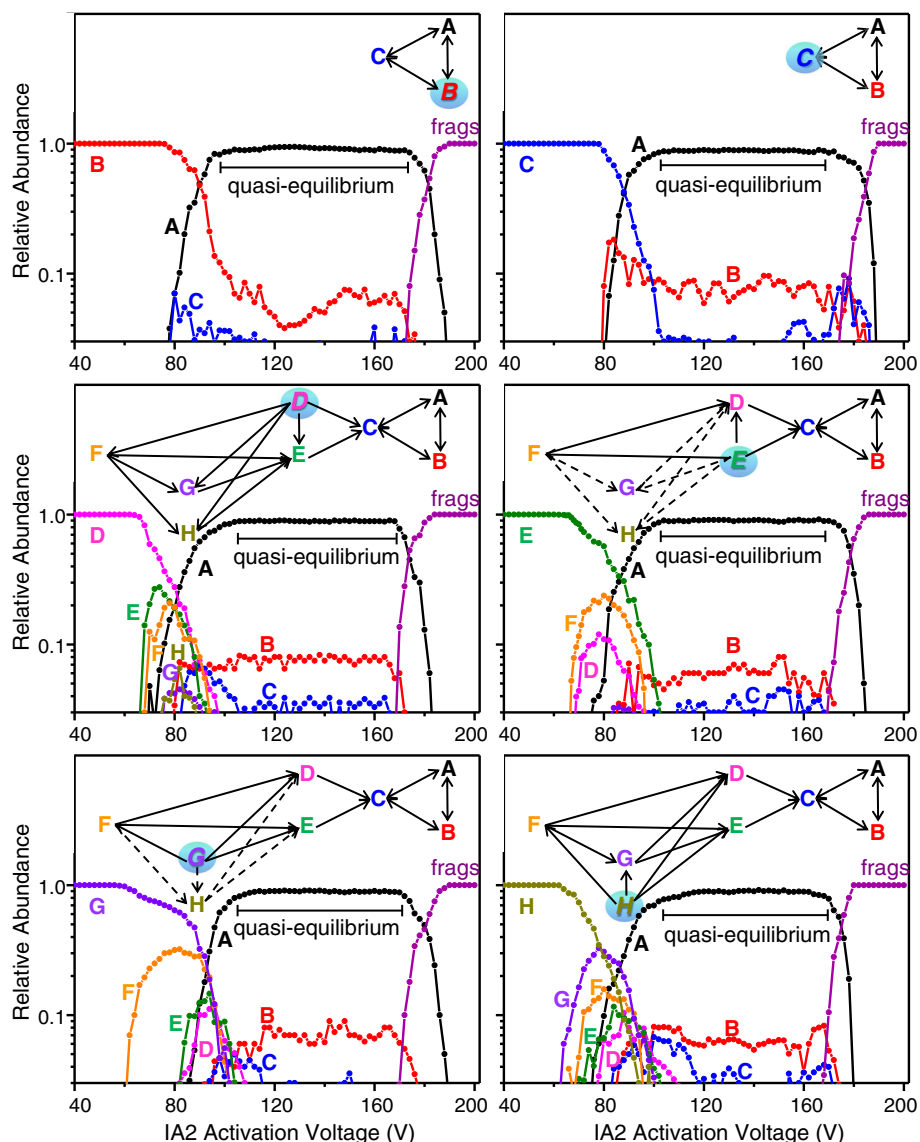


Figure 5. Relative abundance of Pro13 $[M + 2H]^{2+}$ ions as a function of activation voltage when six different solution intermediates are selected and activated: B (top left), C (top right), D (middle left), E (middle right), G (bottom left), and H (bottom right). The observed transition mechanism of each conformer upon activation in vacuo is also shown. A dashed arrow represents a possible transition pathway that may exist but is not observed experimentally. The bracketed line denotes the quasi-equilibrium region prior to fragmentation. Color coding for each conformer is the same as Figure 1, and dark purple represents the relative abundance of all observed fragment populations (frags) originating from the selected ions

activation of B. At higher activation voltages (90, 96, and 98 V), the fraction of conformer B continues to decrease.

Figure 5 shows a similar threshold for formation of conformers A and C from B, at ~ 78 V. Thus, the barriers associated with $B \rightarrow C$ and $B \rightarrow A$ are almost identical. From ~ 80 to ~ 95 V, the population of conformer B decreases quickly, while a sharp increase in conformer A, and a slight increase in the C state, are observed. By ~ 110 V, the quasi-equilibrium distribution of A, B, and C is established. At higher activation voltages (≥ 176 V), the population of fragments increases, and the A–C states disappear. There is no evidence for the presence of more compact structures (conformers D through H), consistent with the transition scheme shown for intermediate B in vacuo.

Selection and Activation of Solution Intermediate C

Selection and activation of conformer C shows a similar trend to that observed for conformers A and B. Example mobility distributions in Figure 4 show that conformers A and B are first observed at 80 V upon activating conformer C. Figure 5 shows the thresholds for $C \rightarrow B$ occur at ~ 79 V and $C \rightarrow A$ at 81 V. That the $C \rightarrow B$ barrier is lower than that for $B \rightarrow A$ is consistent with a reaction sequence $C \rightarrow B \rightarrow A$. The quasi-equilibrium distribution is reached at ~ 110 V, and the ions start to dissociate at ~ 170 V. The folding mechanism of conformer C in vacuo appears to be similar to that found for the A and B peaks.

Selection and Activation of Solution Intermediate D

Transitions of the selected D, E, G, and H states are more complex, similar to the transition found in state F. Figure 4 shows that activation of conformer D leads to the more compact (higher mobility) conformers E, F, G, and H. As the activation voltage reaches 100 V, the fraction of these compact conformers declines, and the ion population is dominated by conformer A. By 120 V, the distributions are essentially identical to those recorded upon activating the A–C states at 120 V, consistent with the establishment of the quasi-equilibrium distribution.

Figure 5 shows the abundances of each observed conformer as a function of activation voltage. Conformer D first converts into conformer E (at ~67 V). At ~68 V, peak F begins to appear. This is interesting. During the $\text{PPI}_{\text{PrOH}} \rightarrow \text{PPII}_{\text{aq}}$ transition in solution, D is an intermediate along the sequential pathway leading to F (PPII_{aq}). That D also forms F in vacuo indicates that some *wet* transitions are accessible in the absence of solvent. Presumably, this $\text{D} \rightarrow \text{F}$ transition is allowed because these structures are similar and exist on regions of the energy landscape that are not restricted by a critical barrier, as is the limitation for A, B, and C transitions to form F.

As the abundance of conformer F decays, there is an increase in the population of the G and H states, suggesting F as a possible intermediate in forming conformers G and H (i.e., $\text{D} \rightarrow \text{F} \rightarrow \text{G}$ and $\text{D} \rightarrow \text{F} \rightarrow \text{H}$, respectively). As soon as the $[\text{PPI} + 2\text{H}]^{2+}$ (peak A) begins to increase, conformers B and C are also observed, and the populations of all intermediate states (E, F, G, and H) decrease. The flat region between 105 V and 165 V corresponds to the A, B, and C quasi-equilibrium. Fragment ions begin to appear at ~170 V.

Based on these results, we propose that the folding of intermediate D in vacuo adopts a similar parallel transition mechanism to that observed for $[\text{PPII} + 2\text{H}]^{2+}$ (peak F). The transition is also analogous to the solution-phase $\text{PPII}_{\text{aq}} \rightarrow \text{PPI}_{\text{PrOH}}$ *dry* folding transition (Figure 1). This parallel mechanism involves a critical barrier to forming the final A, B, and C quasi-equilibrium.

Selection and Activation of Solution Intermediates E, G, and H

Figure 4 shows that the IMS distributions obtained upon activating E, G, and H are similar to those of D and F. Figure 5 shows that activation of conformer E first produces conformer F at 65 V, followed by the formation of conformer D at 67 V. Once conformer A begins to form upon activation at 76 V, a slow increase in the population of conformers B and C is also found. This suggests that conformer E has to overcome a key barrier in order to produce conformers A–C, the local equilibrium populations. With the decay of conformer F, it is also possible that conformers G and H come from F, but with very low efficiency. These data are used to build the transition mechanism of the selected E state in vacuo, a parallel folding mechanism that is also found upon activating peaks F and D.

The abundance profile obtained upon activating conformer G shows that it first converts into conformer F at low activation voltage (~58 V). Once the voltage reaches ~78 V, both conformers D and E appear to form. As the activation voltage is increased, the formation of conformers A–C is found at ~83 V. These results are also consistent with a parallel transition mechanism of the selected G state folding into PPI in vacuo, which involves a key barrier to form the quasi-equilibrium populations. An analogous set of transitions is observed for activation of H (Figure 5).

Folding Landscape of the $\text{PPII} \leftrightarrow \text{PPI}$ Transition Pathway of Pro13 in Vacuo

Based on the data presented above, we can begin to understand the folding landscape associated with the $\text{PPII} \leftrightarrow \text{PPI}$ conformational transitions of Pro13. Figure 6 shows a qualitative folding landscape that is consistent with our experimental findings. It is tempting to interpret our thresholds in terms of activation energy barriers. However, in detailed thermodynamic studies of the dehydration of PPII upon dilution with 1-propanol (i.e., $\text{PPII}_{\text{aq}} \rightarrow \text{PPI}_{\text{PrOH}}$), we found that the reaction was endothermic and driven by an increase in entropy that accompanies nearly every step. Because of this, we do not use a recently developed calibration of these voltages to provide energies [60], instead opting to describe the landscape in terms of the applied voltage necessary to cause each transition.

The PPI helix (peak A) is the most stable gas-phase conformer, as conformer A dominates the quasi-equilibrium distribution. The stability of the PPI helix in vacuo appears to arise from the intrinsic intramolecular forces associated with the helical structure [61], since the dipole moment associated with the helical structure can be maintained in the gas phase. The relative stability of the B and C states is also assessed based on their quasi-equilibrium populations, showing that conformer B is more stable than conformer C. Additionally, upon activation, conformer B produces A and C at the same voltage. This suggests similar barrier heights between $\text{B} \rightarrow \text{C}$ and $\text{B} \rightarrow \text{A}$. The similar conformational changes observed for

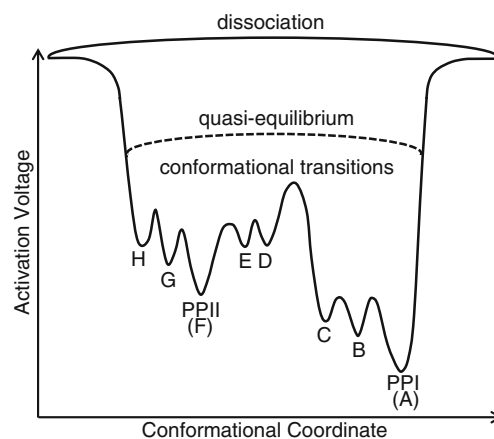


Figure 6. A qualitative folding landscape of the $\text{PPII} \leftrightarrow \text{PPI}$ transitions of Pro13 in vacuo. See text for discussion

conformers A–C also supports the previous structural assignment, wherein conformers B and C are considered to have PPI-like helical structures (Figure 2) [28].

Conformers D through H appear to be less stable than the A–C conformers, as the D–H states are disfavored in the observed quasi-equilibrium distribution. According to the proposed transition pathways in vacuo, conformers D and E appear to have similar conformation changes upon activation. Thus, conformers D and E are considered to be at similar energy levels with a low transition barrier between them. However, the activation barrier of $E \rightarrow F$ should be slightly higher than that of $E \rightarrow D$ because conformer E initially produces F upon activation. Additionally, selection and activation of conformer F leads to formation of G at lower activation than that required to form E, indicating that the barrier height associated with $F \rightarrow E$ is slightly higher than that associated with $F \rightarrow G$. The barrier of $G \rightarrow H$ is assumed to be higher than that of $F \rightarrow G$, as H state can only be produced with very low efficiency in the gas phase. The high barrier between C and D is critical to the folding of Pro13 in vacuo, dividing the population into two primary populations and prohibiting the A–C states from forming any compact structure upon activation. This barrier is higher than the barriers within the A–C group and those within the D–H group, as is shown by the activation voltage required to bring any of the D–H states to a common transition state and produce the quasi-equilibrium populations (conformers A–C).

Conclusions

The gas-phase configurational landscape for Pro13 established here allows us to directly assess solvent effects on the folding of Pro13. Remarkably, the parallel transition mechanism of Pro13 in vacuo involves a critical barrier to form the PPI helix, which is analogous to the PPII \rightarrow PPI folding mechanism observed in 1-propanol, a relatively nonpolar solution environment. The high degree of similarity between transitions observed in the gas phase and in a nonpolar solution environment shows that removal of water is key to producing the all-*cis* PPI helix; but how water is removed—either by solvent exchange or by desolvation during electrospray—does not affect the pathways of Pro13 folding into PPI. The potential energy surface of solution-phase $\text{PPII}_{\text{aq}} \rightarrow \text{PPI}_{\text{PrOH}}$ *dry* folding revealed that in solution, essentially every step of this process is entropically driven [28]. Although more experimental work is required to rigorously delineate the roles of entropy and enthalpy in establishing structures in the gas phase, we cannot resist noting that the remarkable similarity of folding pathways in the nonpolar vacuum and 1-propanol solution requires that in at least some systems the outcome and pathway of folding appears to be intrinsic to the biopolymer. If such behavior extends to other types of environments (e.g., nonpolar surfaces such as membranes) structural measurements and computations of anhydrous biomolecules in vacuo would provide a

grossly simplified means of obtaining structural information—where few condensed-phase options exist.

Acknowledgments

The authors gratefully thank David Smiley and the DiMarchi Laboratory at Indiana University for assistance with the peptide synthesis. This research is supported in part by a grant from the NIH (R01GM103725).

References

- Lummiss, S.C.R., Beene, D.L., Lee, L.W., Lester, H.A., Broadhurst, R.W., Dougherty, D.A.: *Cis-trans* isomerization at a proline opens the pore of a neurotransmitter-gated ion channel. *Nature* **438**, 248–252 (2005)
- Baldwin, R.L.: The search for folding intermediates and the mechanism of protein folding. *Annu. Rev. Biophys.* **37**, 1–21 (2008)
- Sarkar, P., Reichman, C., Saleh, T., Birge, R.B., Kalodimos, C.G.: Proline *cis-trans* isomerization controls autoinhibition of a signaling protein. *Mol. Cell* **25**, 413–426 (2007)
- Crick, S.L., Ruff, K.M., Garai, K., Frieden, C., Pappu, R.V.: Unmasking the roles of N- and C-terminal flanking sequences from exon 1 of huntingtin as modulators of polyglutamine aggregation. *Proc. Natl. Acad. Sci. U. S. A.* **110**, 20075–20080 (2013)
- Caron, N.S., Desmond, C.R., Xia, J., Truant, R.: Polyglutamine domain flexibility mediates the proximity between flanking sequences in huntingtin. *Proc. Natl. Acad. Sci. U. S. A.* **110**, 14610–14615 (2013)
- Morgan, A.A., Rubenstein, E.: Proline: the distribution, frequency, positioning, and common functional roles of proline and polyproline sequences in the human proteome. *PLoS One* **8**, e53785 (2013)
- Li, W., Tailhades, J., O'Brien-Simpson, N.M., Separovic, F., Otvos Jr., L., Hossain, M.A., Wade, J.D.: Proline-rich antimicrobial peptides: potential therapeutics against antibiotic-resistant bacteria. *Amino Acids* **46**, 2287–2294 (2014)
- Cowan, P.M., McGavin, S.: Structure of poly-L-proline. *Nature* **176**, 501–503 (1955)
- Rose, G.D.: Secondary Structure in Protein Analysis. In: Lennarz, W.J., Lane, M.D. (eds.) *Encyclopedia of Biological Chemistry*, vol. 4, pp. 1–6. Academic Press, New York (2013)
- Berg, J.M., Tymoczko, J.L., Stryer, L., Gatto Jr., G.J.: *Biochemistry*. W. H. Freeman and Company, New York (2012)
- Harrington, W.F., Sela, M.: Studies on the structure of poly-L-proline in solution. *Biochim. Biophys. Acta* **27**, 24–41 (1958)
- Kurtz, Z., Berger, A., Katchalski, E.: Mutarotation of poly-L-proline. *Nature* **178**, 1066–1067 (1956)
- Steinberg, I.Z., Harrington, W.F., Berger, A., Sela, M., Katchalski, E.: The configurational changes of poly-L-proline in solution. *J. Am. Chem. Soc.* **82**, 5263–5279 (1960)
- Traub, W., Shmueli, U.: Structure of poly-L-proline I. *Nature* **198**, 1165–1166 (1963)
- Dukor, R.A., Keiderling, T.A.: Mutarotation studies of poly-L-proline using FTIR, electronic and vibrational circular dichroism. *Biospectroscopy* **2**, 83–100 (1996)
- Profant, V., Baumruk, V., Li, X., Šafařík, M., Bouř, P.: Tracking of the polyproline folding by density functional computations and Raman optical activity spectra. *J. Phys. Chem. B* **115**, 15079–15089 (2011)
- Torchia, D.A., Bovey, F.A.: A nuclear magnetic resonance study of poly(L-proline) in aqueous and aqueous salt solutions. *Macromolecules* **4**, 246–251 (1971)
- Lin, L.N., Brandts, J.F.: Kinetic mechanism for conformational transitions between poly-L-prolines I and II: a study utilizing the *cis-trans* specificity of a proline-specific protease. *Biochemistry* **19**, 3055–3059 (1980)
- Moradi, M., Babin, V., Roland, C., Sagui, C.: A classical molecular dynamics investigation of the free energy and structure of short polyproline conformers. *J. Chem. Phys.* **133**, 125104–125122 (2010)
- Moradi, M., Babin, V., Roland, C., Darden, T.A., Sagui, C.: Conformations and free energy landscapes of polyproline peptides. *Proc. Natl. Acad. Sci. U. S. A.* **106**, 20746–20751 (2009)

21. Moradi, M., Lee, J.G., Babin, V., Roland, C., Sagui, C.: An ab initio and classical molecular dynamics investigation. *Int. J. Quantum Chem.* **110**, 2865–2879 (2010)
22. Chiang, Y., Lin, Y., Horng, J.: Stereoelectronic effects on the transition barrier of polyproline conformational interconversion. *Protein Sci.* **18**, 1967–1977 (2009)
23. Lu, K.P., Finn, G., Lee, T.H., Nicholson, L.K.: Prolyl *cis-trans* isomerization as a molecular timer. *Nat. Chem. Biol.* **3**, 619–629 (2007)
24. Schimmel, P.R., Flory, P.J.: Conformational energy and configurational statistics of poly-L-proline. *Proc. Natl. Acad. Sci. U. S. A.* **58**, 52–59 (1967)
25. Swenson, C.A., Formanek, R.: Infrared study of poly-L-proline in aqueous solution. *J. Phys. Chem.* **71**, 4073–4077 (1967)
26. Forsythe, K.H., Hopfinger, A.J.: The influence of solvent on the secondary structures of poly(l-alanine) and poly(l-proline). *Macromolecules* **6**, 423–437 (1973)
27. Shi, L., Holliday, A.E., Shi, H., Zhu, F., Ewing, M.A., Russell, D.H., Clemmer, D.E.: Characterizing intermediates along the transition from PPI to PPII using ion mobility-mass spectrometry. *J. Am. Chem. Soc.* **136**, 12702–12711 (2014)
28. Shi, L., Holliday, A.E., Glover, M.S., Ewing, M.A., Russell, D.H., Clemmer, D.E.: Ion mobility-mass spectrometry reveals the energetics of intermediates that guide polyproline folding. *J. Am. Soc. Mass Spectrom.* **27**, 22–30 (2016)
29. Fenn, J.B., Mann, M., Meng, C.K., Wong, S.F., Whitehouse, C.M.: Electrospray ionization for mass spectrometry of large biomolecules. *Science* **246**, 64–71 (1989)
30. Ruotolo, B.T., Giles, K., Campuzano, I., Sandercock, A.M., Bateman, R.H., Robinson, C.V.: Evidence for macromolecular protein rings in the absence of bulk water. *Science* **310**, 1658–1661 (2005)
31. Ruotolo, B.T., Robinson, C.V.: Aspects of native proteins are retained in vacuum. *Curr. Opin. Chem. Biol.* **10**, 402–408 (2006)
32. Bleiholder, C., Do, T.D., Wu, C., Economou, N.J., Bernstein, S.S., Buratto, S.K., Shea, J.-E., Bowers, M.T.: Ion mobility spectrometry reveals the mechanism of amyloid formation of A β (25–35) and its modulation by inhibitors at the molecular level: epigallocatechin gallate and scyllo-inositol. *J. Am. Chem. Soc.* **135**, 16926–16937 (2013)
33. Loo, J.A., Edmonds, C.G., Smith, R.D.: Primary sequence information from intact proteins by electrospray ionization tandem mass spectrometry. *Science* **248**, 201–204 (1990)
34. Merenbloom, S.I., Flick, T.G., Williams, E.R.: How hot are your ions in T-wave ion mobility spectrometry? *J. Am. Soc. Mass Spectrom.* **23**, 553–562 (2012)
35. Wytenbach, T., Bowers, M.T.: Structural stability from solution to the gas phase: native solution structure of ubiquitin survives analysis in a solvent-free ion mobility-mass spectrometry environment. *J. Phys. Chem. B* **115**, 12266–12275 (2011)
36. Wytenbach, T., Pierson, N.A., Clemmer, D.E., Bowers, M.T.: Ion mobility analysis of molecular dynamics. *Annu. Rev. Phys. Chem.* **65**, 175–196 (2014)
37. Nagornova, N.S., Rizzo, T.R., Boyarkin, O.V.: Interplay of intra- and intermolecular H-bonding in a progressively solvated macrocyclic peptide. *Science* **336**, 320–323 (2012)
38. Garand, E., Kamrath, M.Z., Jordan, P.A., Wolk, A.B., Leavitt, C.M., McCoy, A.B., Miller, S.J., Johnson, M.A.: Determination of noncovalent docking by infrared spectroscopy of cold gas-phase complexes. *Science* **335**, 694–698 (2012)
39. Prell, J.S., Corra, T.C., Chang, T.M., Biles, J.A., Williams, E.R.: Entropy drives an attached water molecule from the C- to N-terminus on protonated proline. *J. Am. Chem. Soc.* **132**, 14733–14735 (2010)
40. Prell, J.S., Chang, T.M., O’Brien, J.T., Williams, E.R.: Hydration isomers of protonated phenylalanine and derivatives: relative stabilities from infrared photodissociation. *J. Am. Chem. Soc.* **132**, 7811–7819 (2010)
41. Gross, D.S., Schnier, P.D., Rodriguez-Cruz, S.E., Fagerquist, C.K., Williams, E.R.: Conformations and folding of lysozyme ions in vacuo. *Proc. Natl. Acad. Sci. U. S. A.* **93**, 3143–3148 (1996)
42. Bohrer, B.C., Merenbloom, S.I., Koeniger, S.L., Hilderbrand, A.E., Clemmer, D.E.: Biomolecule Analysis by Ion Mobility Spectrometry. *Annu. Rev. Anal. Chem.* **1**, 293–327 (2008)
43. McLean, J.A., Ruotolo, B.T., Gillig, K.J., Russell, D.H.: Ion mobility-mass spectrometry: a new paradigm for proteomics. *Int. J. Mass Spectrom.* **240**, 301–315 (2005)
44. Tang, K., Shvartsburg, A.A., Lee, H.-N., Prior, D.C., Buschbach, M.A., Li, F., Tolmachev, A.V., Anderson, G.A., Smith, R.D.: High-sensitivity ion mobility spectrometry/mass spectrometry using electrodynamic ion funnel interfaces. *Anal. Chem.* **77**, 3330–3339 (2005)
45. Kanu, A.B., Dwivedi, P., Tam, M., Matz, L., Hill Jr., H.H.: Ion mobility-mass spectrometry. *J. Mass Spectrom.* **43**, 1–22 (2008)
46. Mason, E.A., McDaniel, E.W.: Transport properties of ions in gases. Wiley, New York (1988)
47. Revercomb, H.E., Mason, E.A.: Theory of plasma chromatography/gaseous electrophoresis. *Anal. Chem.* **47**, 970–983 (1975)
48. Mesleh, M.F., Hunter, J.M., Shvartsburg, A.A., Schatz, G.C., Jarrold, M.F.: Structural information from ion mobility measurements: effects of the long-range potential. *J. Phys. Chem.* **100**, 16082–16086 (1996)
49. Shvartsburg, A.A., Jarrold, M.F.: An exact hard-spheres scattering model for the mobilities of polyatomic ions. *Chem. Phys. Lett.* **261**, 86–91 (1996)
50. Wytenbach, T., von Helden, G., Batka, J.J., Carlat, D., Bowers, M.T.: Effect of the long-range potential on ion mobility measurements. *J. Am. Soc. Mass Spectrom.* **8**, 275–282 (1997)
51. Wytenbach, T., Bleiholder, C., Bowers, M.T.: Factors contributing to the collision cross section of polyatomic ions in the kilodalton to gigadalton range: application to ion mobility measurements. *Anal. Chem.* **85**, 2191–2199 (2013)
52. Bleiholder, C., Wytenbach, T., Bowers, M.T.: A novel projection approximation algorithm for the fast and accurate computation of molecular collision cross sections. (I). *Method. Int. J. Mass Spectrom.* **308**, 1–10 (2011)
53. Shaffer, S.A., Tang, K.Q., Anderson, G.A., Prior, D.C., Udseth, H.R., Smith, R.D.: A novel ion funnel for focusing ions at elevated pressure using electrospray ionization mass spectrometry. *Rapid Commun. Mass Spectrom.* **11**, 1813–1817 (1997)
54. Hoaglund, C.S., Valentine, S.J., Sporleder, C.R., Reilly, J.P., Clemmer, D.E.: Three-dimensional ion mobility/TOFMS analysis of electrosprayed biomolecules. *Anal. Chem.* **70**, 2236–2242 (1998)
55. Koeniger, S.L., Merenbloom, S.I., Clemmer, D.E.: Evidence for many resolvable structures within conformation types of electrosprayed ubiquitin ions. *J. Phys. Chem. B* **110**, 7017–7021 (2006)
56. Koeniger, S.L., Merenbloom, S.I., Valentine, S.J., Jarrold, M.F., Udseth, H.R., Smith, R.D., Clemmer, D.E.: An IMS-IMS analogue of MS-MS. *Anal. Chem.* **78**, 4161–4174 (2006)
57. Merenbloom, S.I., Koeniger, S.L., Valentine, S.J., Plasencia, M.D., Clemmer, D.E.: IMS-IMS and IMS-IMS-IMS/MS for separating peptide and protein fragment ions. *Anal. Chem.* **78**, 2802–2809 (2006)
58. Pierson, N.A., Valentine, S.J., Clemmer, D.E.: Evidence for a quasi-equilibrium distribution of states for bradykinin $[M + 3H]^{3+}$ ions in the gas phase. *J. Phys. Chem. B* **114**, 7777–7783 (2010)
59. Chandrudu, S., Simerska, P., Toth, I.: Chemical methods for peptide and protein production. *Molecules* **18**, 4373–4388 (2013)
60. Pierson, N.A., Clemmer, D.E.: An IMS-IMS threshold method for semi-quantitative determination of activation barriers: Interconversion of proline *cis*→*trans* forms in triply protonated bradykinin. *Int. J. Mass Spectrom.* **377**, 646–654 (2015)
61. Kuemin, M., Schweizer, S., Ochsenfeld, C., Wennemers, H.: Effects of terminal functional groups on the stability of the polyproline II structure: a combined experimental and theoretical study. *J. Am. Chem. Soc.* **131**, 15474–15482 (2009)